

Tall-building effects on pedestrian-level flow and pollutant dispersion: Large-eddy simulations

Jong-Won Kim^a, Jong-Jin Baik^{a,*}, Beom-Soon Han^b, Joohyun Lee^a, Han-Gyul Jin^a,
Kyeongjoo Park^a, Hyeji Yang^a, Seung-Bu Park^c

^a School of Earth and Environmental Sciences, Seoul National University, Seoul, South Korea

^b Department of Environment and Energy, Semyung University, Jecheon, Chungcheongbuk-do, South Korea

^c School of Environmental Engineering, University of Seoul, Seoul, South Korea



ARTICLE INFO

Keywords:

Flow
Pollutant dispersion
Air quality
Pedestrian level
Tall building
Large-eddy simulation

ABSTRACT

The urban environmental impact of tall buildings has increasingly become an important topic of investigation, with the rapid pace of tall-building constructions around the world. In this study, the effects of a tall building on pedestrian-level flow and pollutant dispersion are investigated using the parallelized large-eddy simulation model (PALM). Numerical simulations are conducted by changing the tall-building height in the configuration of a tall building surrounded by low-rise cubical buildings. As the tall-building height increases, the time- and area-averaged pedestrian-level wind speed and pollutant concentration increases and decreases, respectively. Both the rates of changes in the average wind speed and pollutant concentration decrease with increasing tall-building height. The trend of the average wind speed is attributable to an increasing tendency of oncoming flows to pass by the sides of the tall building rather than going down as the tall-building height increases. The trend of the average pollutant concentration is associated with that of the average wind speed. Instantaneous flow and pollutant dispersion are also analyzed. In the upstream region of the tall building, bulks of polluted air are repeatedly transported from further upstream regions and enter the canyon right in front of the tall building, temporarily increasing the pedestrian-level pollutant concentration near the windward wall of the tall building. In the downstream region of the tall building, at the pedestrian level, two counter-rotating vortices appear in the canyon just behind the tall building. Each of these vortices repeatedly develops at one of the two leeward corners of the tall building, moves downstream while changing its size, and disappears after reaching the windward wall of the neighboring low-rise building. These coherent vortices considerably affect the spatiotemporal variation of pedestrian-level pollutant concentration in the canyon just behind the tall building.

1. Introduction

Urban air pollution has been considered an important environmental issue, which causes adverse impacts on human health and ecosystem (Grantz et al., 2003; Kampa and Castanas, 2008; Kim et al., 2015; Stevens et al., 2020). In urban areas, buildings of various sizes and shapes and their inhomogeneous spatial distribution make flow and associated pollutant dispersion at microscale quite complex. To properly cope with urban air pollution problem, it is necessary to have much understanding of microscale flow and pollutant dispersion in urban areas. One way of understanding them is through building-resolving numerical simulations for idealized as well as real urban settings.

Flow and pollutant dispersion in building arrays have been extensively investigated through numerical simulations. Buccolieri et al. (2010) showed that as the building plan area density increases, the recirculations within the building array strengthen and accordingly the ventilation efficiency becomes low. Hang et al. (2012) demonstrated that pollutant dispersion at the pedestrian level is enhanced with increasing building height variability. Razak et al. (2013) found that the area-averaged pedestrian-level wind speed exponentially decreases as the building frontal area density increases. Mei et al. (2017) showed that for a fixed building plan area density, reduction of building frontal area density increases the ventilation by enhancing the roof-level air exchange rate. These studies indicate that urban morphological factors

Peer review under responsibility of Turkish National Committee for Air Pollution Research and Control.

* Corresponding author. School of Earth and Environmental Sciences, Seoul National University, Seoul 08826, South Korea.

E-mail address: jjbalk@snu.ac.kr (J.-J. Baik).

such as building plan area density, building frontal area density, and building height variability significantly influence flow and pollutant dispersion.

When a tall building is constructed within an area of low-rise buildings, local building frontal density and building height variability are increased and pollutant dispersion can be enhanced due to strong downdrafts and updrafts near the windward and leeward walls of the tall building, respectively (Brixey et al., 2009; Fuka et al., 2018; Heist et al., 2009; Huang et al., 2021). Recently, tall buildings have been increasingly built around the world. The number of buildings higher than 300 m increased from 24 in 2000 to 180 in 2020 (CTBUH). The accelerated pace of tall-building constructions necessitates a better understanding of tall-building effects on near-surface wind and air quality. There are some numerical simulation studies of tall-building effects on flow and pollutant dispersion. For example, Brixey et al. (2009) showed that pollutants behind a tall building disperse faster as its height increases. Tamura et al. (2019) found that in the case of an isolated tall building, the maximum increase in the pedestrian-level wind speed due to the presence of a tall building logarithmically increases with increasing tall-building height. In association with the study of Tamura et al. (2019), it would be interesting to examine how the pedestrian-level wind speed and pollutant concentration vary as the height of a tall building surrounded by low-rise buildings increases.

Previous numerical simulation studies of tall-building effects on pollutant dispersion have mostly focused on time-averaged fields (e.g., Huang et al., 2021). Considering highly transient nature of flow and associated pollutant dispersion in built-up urban areas, it is important to have an in-depth understanding of instantaneous flow or flow structure and its role in pollutant dispersion. Through the detailed analysis of instantaneous flow and pollutant concentration fields, Park et al. (2022) showed that the combination of various coherent flow structures in a street canyon that are connected to each other drives in-canyon pollutant dispersion. Their study investigated flow and pollutant dispersion in a two-dimensional array of equal-height buildings, where coherent flow structures may similarly appear in street canyons. In a setting of a tall building surrounded by low-rise buildings, flow structures in the windward side of the tall building will be different from those in its leeward side. It would be challenging to identify flow structures in the windward and leeward sides of the tall building and examine how the flow structures in each side affect the distribution of pollutants, particularly at the pedestrian level.

In this study, we investigate tall-building effects on flow and pollutant dispersion, focusing on the level where pedestrians are exposed to harmful pollutants. For this, an idealized setting with a tall building surrounded by low-rise buildings is considered and a large-eddy simulation (LES) model is used. In section 2, the LES model and simulation design are described. In section 3, the LES model is validated against the wind tunnel experiment data. Then, simulation and analysis results are presented and discussed. A summary and conclusions are given in section 4.

2. LES model and simulation design

In this study, the parallelized LES model (PALM) version 6.0 is used (Maronga et al., 2020; Raasch and Schröter, 2001). PALM solves implicitly filtered prognostic equations for velocity components, passive scalar concentration, and subgrid-scale turbulent kinetic energy (TKE). The upwind-biased fifth-order differencing scheme (Wicker and Skamarock, 2002) is used for discretization of advection terms, and the third-order Runge-Kutta differencing scheme (Williamson, 1980) is used for time integration. For the parameterization of subgrid-scale turbulent fluxes, the 1.5-order Deardorff closure scheme (Deardorff, 1980) modified by Moeng and Wyngaard (1988) and Saiki et al. (2000) is applied.

The computational domain size is 900 m in the x (streamwise) direction, 360 m in the y (spanwise) direction, and 551 m in the z (vertical)

direction (Fig. 1a). The grid size is 1 m both in the x and y directions. The grid size in the z direction is 1 m up to $z = 150$ m, and above that level, it is gradually stretched with an expansion ratio of 1.08. An array of cubical buildings with a height of 20 m (H) is considered as the basic building configuration in this study. In the building array, a total of 153 (17 (x) \times 9 (y)) cubical buildings are regularly aligned with a constant spacing of 20 m both in the x and y directions. The cubical building array is located 100 m and 140 m away from the inflow and outflow boundaries ($x = 0$ m and 900 m), respectively. To examine the effects of a tall building on flow and pollutant dispersion and how they vary with the height of the tall building, five simulations with different heights of a target building centered at $(x, y) = (350 \text{ m}, 180 \text{ m})$, ranging from 20 m to 100 m at intervals of 20 m, are conducted. The five simulation cases are named after the height of the target building, that is, the 1H, 2H, 3H, 4H, and 5H cases. The computational domain and building configuration for the 5H case are shown in Fig. 1a. Note that six and ten rows of cubical buildings exist in front of and behind the target building, respectively. Although the target building is not taller than other buildings in the 1H case, the height of the target building is referred to as the tall-building height in this study for convenience.

The stationary profile generated from a one-dimensional model

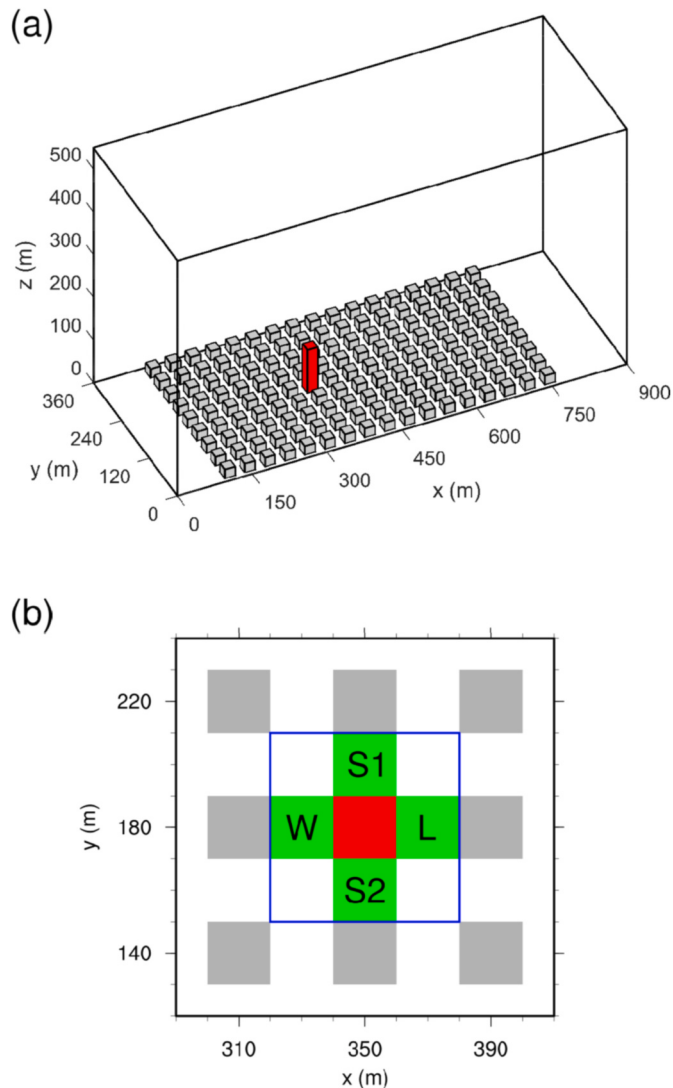


Fig. 1. Illustrations of (a) the computational domain and building configuration and (b) the horizontal cross-section near the tall building. The height of the red building centered at the point $(x, y) = (350 \text{ m}, 180 \text{ m})$ in (a) varies from 20 m to 100 m at intervals of 20 m.

where the initial wind profile is vertically uniform at 6 m s^{-1} is used as the inflow profile in the simulations. The generated inflow profile exhibits an increase with height; the wind speed is 2.01 m s^{-1} at $z = 20 \text{ m}$ and 3.01 m s^{-1} at $z = 100 \text{ m}$. The Dirichlet and radiation boundary conditions are applied at the inflow and outflow boundaries, respectively, and the cyclic boundary condition is applied at the lateral boundaries ($y = 0 \text{ m}$ and 360 m). The zero-gradient boundary condition is applied at the top boundary. The Coriolis effect is not considered in this study. Non-reactive pollutants are emitted from every grid point at the street bottom surface with a constant scalar flux (q) of $1 \mu\text{g m}^{-2} \text{s}^{-1}$, which is similar to the measured emission rates of NO_x in a megacity reported by Squires et al. (2020). The LES model is integrated for 90 min, and the last 900 s data with 2-s intervals are used for analysis.

3. Results and discussion

3.1. Model validation

To evaluate PALM's capability to simulate flows around a tall building, a simulation that imitates a benchmark wind tunnel experiment by the Architectural Institute of Japan (AIJ) (2016) is conducted. The building configuration of a tall building surrounded by low-rise buildings resembles that in our large-eddy simulations. The wind tunnel experiment data provided in AIJ (2016) focuses on the pedestrian-level wind environment around the buildings, which also matches the objective of this study. Fig. S1a shows the configuration of the simulation. A tall building is surrounded by low-rise buildings. In this scale-up simulation, the sizes of the tall building and low-rise buildings are $25 \text{ m} (x) \times 25 \text{ m} (y) \times 100 \text{ m} (z)$ and $40 \text{ m} \times 40 \text{ m} \times 10 \text{ m}$, respectively. The wind profile based on 13 data points provided in AIJ (2016) is applied as the inflow boundary condition of the simulation. More details of the experiment setup are given in AIJ (2016). The normalized wind speed is calculated at each point by dividing wind speed near the ground surface by the inflow wind speed at the height of the tall building, and it is used for validation.

Fig. S1b shows 78 measurement points near the tall building in the wind tunnel experiment. Near-ground measurement data obtained from thermistor anemometers are used for the model validation. The data at 12 points adjacent to the tall building are not available, and these points are marked by black dots. The colors of the other points indicate the ratio of the normalized wind speed in the simulation to that in the wind tunnel experiment. In the upwind region (the left side of the tall building), the normalized wind speeds in the simulation are larger than those in the wind tunnel experiments near the windward wall of the tall building, while they are smaller near the corners of the neighboring buildings. In the downwind region (the right side of the tall building), the normalized wind speeds in the simulation tend to be smaller than those in the wind tunnel experiment, although there are exceptions. In the side regions of the tall building, the normalized wind speeds in the simulation and wind tunnel experiment well match each other. The accuracy of the simulation is high at the points with high normalized wind speeds (Fig. S1c). AIJ (2016) also noted that computational fluid dynamics model simulations showed high accuracy at the points with high normalized wind speeds. Overall, normalized wind speeds in the simulation are well correlated with those in the wind tunnel experiment, with a correlation coefficient of 0.79. The validation results show that PALM is capable of reasonably simulating winds near a tall building surrounded by low-rise buildings. It is noted that the capability of PALM to simulate turbulent flow and pollutant dispersion has been evaluated for idealized building configurations (Han et al., 2018; Park et al., 2013; Wang and Ngan, 2021) and for real urban settings (Resler et al., 2021). For example, Han et al. (2018) compared the vertical profile of simulated scalar concentration with that of wind tunnel experiment and confirmed that PALM is a reliable model for investigating turbulent flow and associated pollutant dispersion.

3.2. Mean flow and pollutant concentration

Fig. 2 shows fields of time-averaged wind speed and wind vector on the x - z plane at $y = 180 \text{ m}$ and on the x - y plane at $z = 1.5 \text{ m}$ (a pedestrian level) in the 1H, 2H, 3H, 4H, and 5H cases. In this study, the time average is taken over the last 900 s. There are two methods for averaging wind speed: averaging instantaneous wind speeds and calculating the magnitude of averaged wind vector (AIJ, 2016; Kikumoto et al., 2018; Tominaga et al., 2004). In this study, the former is used. In the 1H case where the heights of all buildings are equal, flows mostly pass over the canyons rather than entering them (Fig. 2a). Below $z = H$, a weak clockwise vortex appears in each canyon (it was confirmed through a streamline field). At the pedestrian level, the wind is very weak (Fig. 2b).

In the 2H, 3H, 4H, and 5H cases where one building is taller than the others, there are regions of downdrafts and updrafts near the windward and leeward walls of the tall building, respectively. Oncoming flows blocked by the tall building diverge from a stagnation point on the windward wall of the tall building (marked by yellow dots in Fig. 2c, e, g, and i). Here, the stagnation point is the point where the velocity is zero. Downdrafts occur below the height of the stagnation point and have a maximum intensity below $z = H$. In the canyon between the tall building and the neighboring low-rise building located upstream of the tall building ($320 \text{ m} < x < 340 \text{ m}$), a clockwise vortex appears (Fig. 2c, e, g, and i), similar to the 1H case but with a stronger intensity. The simulated downdrafts and vortex are similar to those in Fuka et al. (2018) and Heist et al. (2009). In the canyon between the tall building and the neighboring low-rise building located downstream of the tall building ($360 \text{ m} < x < 380 \text{ m}$), there are upward flows directing toward the tall building (Fig. 2c, e, g, and i). At further downstream, two branches of upward flows are seen above $z \sim H$; one is in the downstream direction, and the other is nearly upright at the levels close to $z \sim H$ and gradually turns toward the tall building with height.

To examine the horizontal flows around the tall building, we name four regions between the tall building and neighboring low-rise buildings W, L, S1, and S2 (see Fig. 1b). W, L, and S1 (S2) stand for the windward, leeward, and lateral sides of the tall building, respectively. In the 2H, 3H, 4H, and 5H cases, at the pedestrian level, strongly diverging horizontal flows are seen in W (Fig. 2d, f, h, and j), which is attributable to downdrafts near the windward wall of the tall building. High-speed flows almost symmetric with respect to $y = 180 \text{ m}$ pass through S1 and S2. The flow speed is especially high near the leeward-wall corners of the tall building. Near-ground high-speed flows near the lateral sides of a tall building were also reported in an LES study over a real urban area (Park et al., 2015). In L, two counter-rotating vortices are seen, which produce a strong flow toward the leeward wall of the tall building.

Although the flow fields in the 2H, 3H, 4H, and 5H cases share common features such as downdrafts near the windward wall of the tall building, updrafts near its leeward wall, and high-speed flows in S1 and S2, their size and intensity change with the tall-building height. For example, the vertical size of the region of the downdrafts near the windward wall of the tall building increases almost linearly with the tall-building height (Fig. 2c, e, g, and i). The intensity of the high-speed flow at $z = 1.5 \text{ m}$ also increases with the tall-building height, but the rate of increase decreases with the tall-building height (Fig. 2d, f, h, and j). The intensity of the high-speed flow noticeably increases from the 2H case to the 3H case, while it does not change much from the 4H case to the 5H case.

The time- and area-averaged wind speed at the pedestrian level ($z = 1.5 \text{ m}$) as a function of tall-building height is shown in Fig. 3a. The area average is taken over the $60 \text{ m} \times 60 \text{ m}$ square region around the tall building (the blue square in Fig. 1b). The tall-building height is normalized by H , and the average wind speed is normalized by U_H which is the inflow speed at $z = H$. The average pedestrian-level wind speed increases with increasing tall-building height, but the rate of increase in

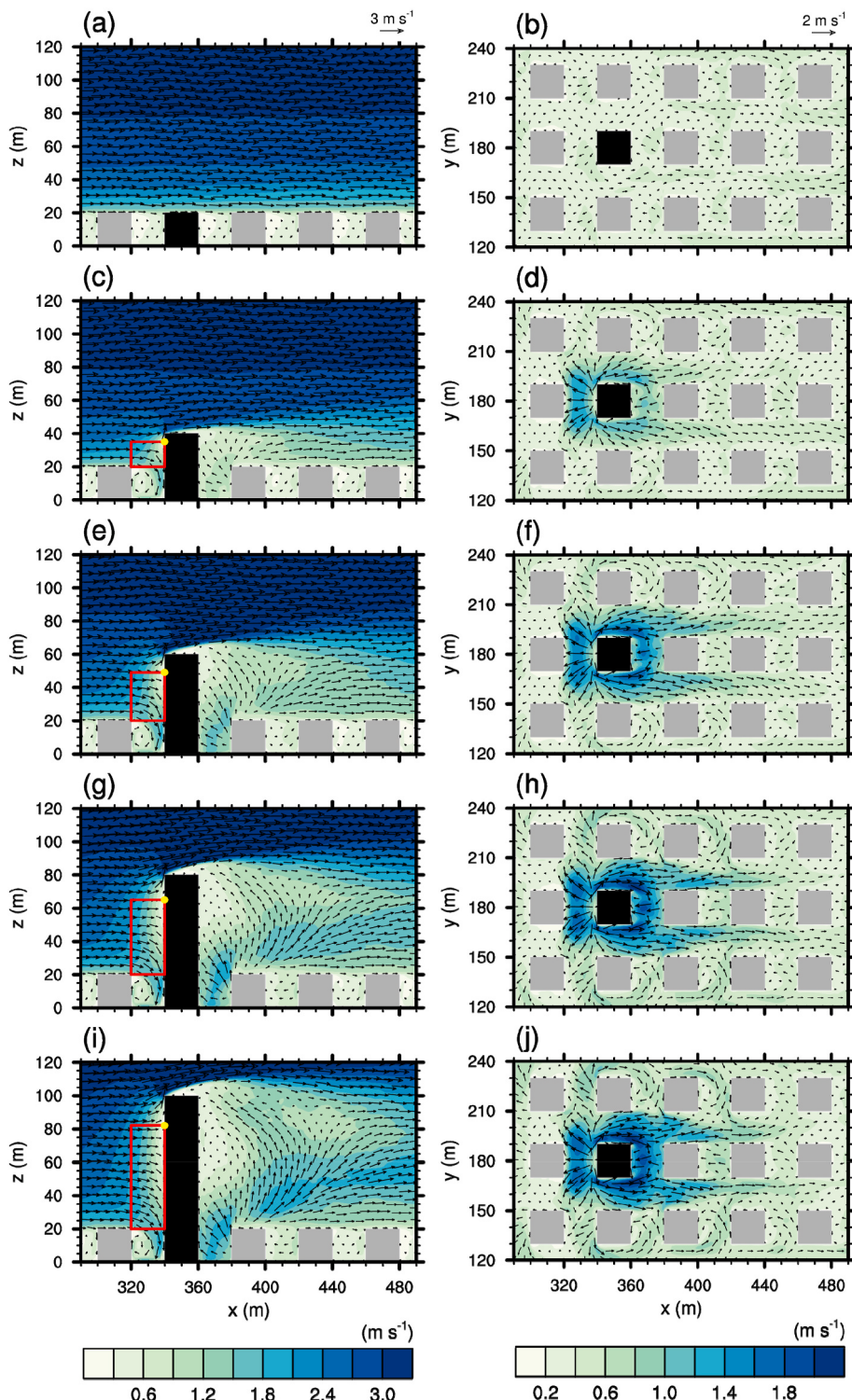


Fig. 2. Fields of time-averaged wind speed and wind vector on the x - z plane at $y = 180$ m (left column) and on the x - y plane at $z = 1.5$ m (right column) in the (a, b) 1H, (c, d) 2H, (e, f) 3H, (g, h) 4H, and (i, j) 5H cases. The blocks in black indicate the tall buildings. The yellow dots indicate stagnation points on the windward walls of the tall buildings. The red solid line in each of (c), (e), (g), and (i) indicates the boundary of a column for calculating the flow rate.

the average wind speed decreases with increasing tall-building height. A regression analysis finds a fitting curve of $y = 0.669 - 1.024 \exp(-0.711x)$ (Fig. 3a), with the coefficient of determination being 0.999. We performed additional two simulations with tall-building heights of 6H and 7H and found that the data points for the two simulations almost perfectly lie on the fitting curve. Fig. 2 and the fitting curve indicate that the effect of the increase in the tall-building height on the pedestrian-

level wind speed exponentially weakens with the tall-building height and that for high enough tall buildings (e.g., 5H, 6H, and 7H), their effects are similar.

To get insights into the exponential trend of the average pedestrian-level wind speed with the tall-building height, the volumetric flow rates for a column (marked by red lines in Fig. 2) over W are calculated for each case. The flow rate at each surface (Q) is given by:

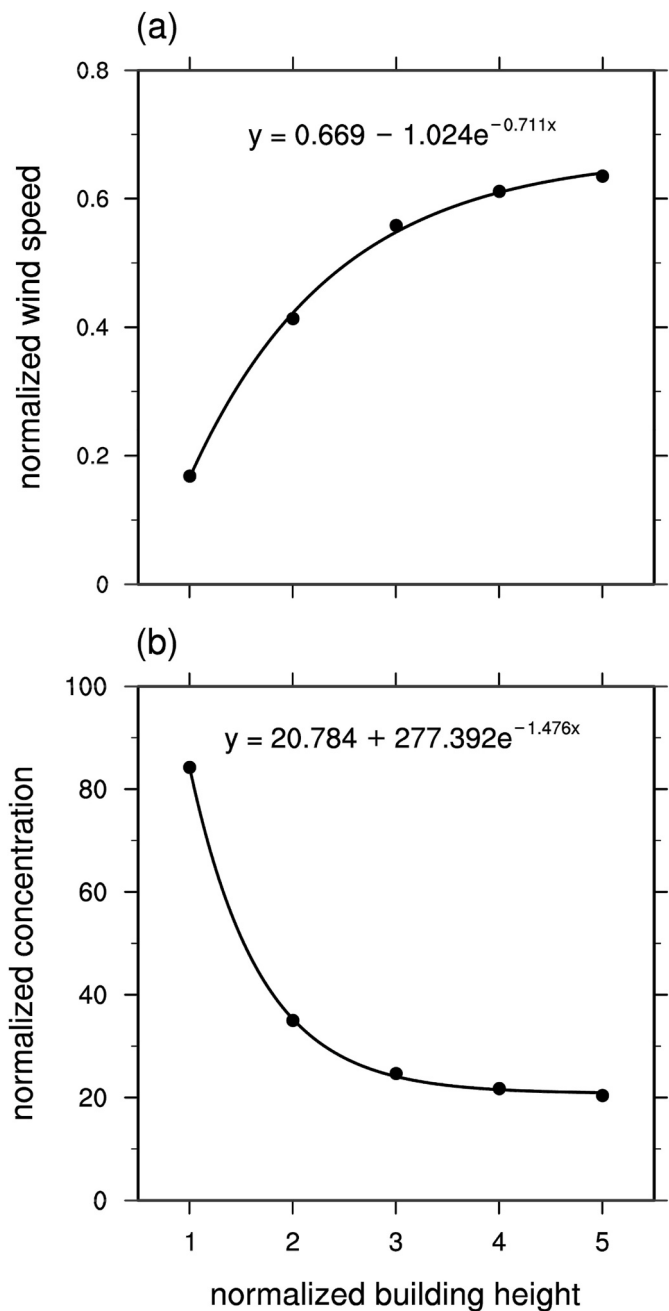


Fig. 3. Time- and area-averaged (a) wind speed and (b) pollutant concentration near the tall building at $z = 1.5$ m as a function of tall-building height. The tall-building height is normalized by H . The average wind speed and pollutant concentration are normalized by U_H and q/U_H , respectively. The black solid lines are fitted curves.

$$Q = \int_A \mathbf{V} \cdot \mathbf{n} dA \quad (1)$$

where \mathbf{V} is the flow velocity, \mathbf{n} is the unit vector normal to the surface, and A is the surface area. The unit vector normal to the front surface of the column directs inward, while those normal to the bottom surface and two side surfaces of the column direct outward. Flows passing through the front surface of the column exit through the two side surfaces or the bottom surface. The column in each case vertically extends from $z = 20$ m to the height of the stagnation point with a horizontal size of $20 \text{ m} \times 20 \text{ m}$. The heights of the stagnation points in the 2H, 3H, 4H, and 5H cases are 35, 49, 65, and 82 m which are 0.88, 0.82, 0.81, and 0.82 times

the tall-building height, respectively. Among the closest points to the windward wall of the tall building with $(x, y) = (339.5 \text{ m}, 180 \text{ m})$, the two consecutive grid points with positive vertical velocity at the upper one and negative vertical velocity at the lower one are identified, and the height of the upper one is selected as the height of the stagnation point for each case.

The calculated flow rates and their ratios as a function of tall-building height are presented in Fig. 4. Note that the flow rate in Fig. 4b is the sum of flow rates at the two side surfaces and that the flow rates at the two side surfaces are nearly the same. The net flow rate at the top surface is $\sim 1.9\text{--}3.0\%$ of the front-surface flow rate for the four cases, which is very small compared to those at the other surfaces. As the tall-building height increases, the front-surface and side-surface flow rates increase almost linearly (Fig. 4a and b). The increase in the front-surface flow rate is associated with the surface area of the windward wall increasing with the tall-building height. The bottom-surface flow rate also increases with increasing tall-building height, but the increasing rate decreases with increasing tall-building height (Fig. 4c). This tendency at the bottom surface is similar to that of the average pedestrian-level wind speed shown in Fig. 3a. For a given tall-building height, the front-surface flow rate is, as should be, the largest, the side-surface flow rate is larger than the bottom-surface flow rate, and the front-surface flow rate is approximately equal to the sum of the side-surface and bottom-surface flow rates. The ratios of the side-surface flow rate to the front-surface flow rate and the ratios of the bottom-surface flow rate to the front-surface flow rate (Fig. 4d) show that as the building height increases, the tendency of flows entering through the front surface to exit through the side surfaces rather than the bottom surface increases (Fig. 4d). The ratio of the bottom-surface flow rate to the front-surface flow rate decreases from 0.46 in the 2H case to 0.15 in the 5H case. On the other hand, the ratio of the side-surface flow rate to the front-surface flow rate increases from 0.50 in the 2H case to 0.80 in the 5H case. In short, as the tall-building height increases, the oncoming flows have a greater tendency to pass by the sides of the tall building. Thus, the rate of increase in the amount of the flows going downward decreases with increasing tall-building height, which results in the trend of the average pedestrian-level wind speed (Fig. 3a).

Our analysis results are consistent with the explanation by Tamura et al. (2019) who reported a similar tendency for the maximum increase in the pedestrian-level wind speed due to the presence of an isolated tall building. However, it is noteworthy that Tamura et al. (2019) selected a logarithmic fitting curve to approximate the tendency rather than the exponential fitting curve selected in this study. The two curves differ from each other in that the exponential curve converges to a certain value for high enough tall building heights, while the logarithmic curve does not. For the simulation results in this study, the exponential fitting curve yields a slightly higher coefficient of determination (0.999) than the logarithmic curve (0.992). The appropriate form of the fitting curve may change with simulation settings such as the building configuration and inflow profile, which deserves further investigation.

Fields of time-averaged pollutant concentration corresponding to Fig. 2 are shown in Fig. 5. In the 1H case, the pollutant concentration is higher near the leeward wall of a building than near its windward wall (Fig. 5a), as reported in many previous studies (e.g., Santiago et al., 2007). At the pedestrian level (Fig. 5b), the pollutant concentration is lower near the windward wall than near the leeward wall. It is interesting to observe that near the leeward wall, the pollutant concentration tends to be locally high near one of the two leeward corners. This is associated with pollutant trapping by a vortex near one of the two leeward corners.

In the 2H, 3H, 4H, and 5H cases, relatively strong downdrafts near the windward wall of the tall building draw relatively clean air down in W (Fig. 5c, e, g, and i). Pollutants are transported upward by the upward motion over the canyon just behind the tall building. Accordingly, compared with the 1H case, the pollutant concentration in the canyon decreases, while the pollutant concentration above $z \sim 40$ m increases.

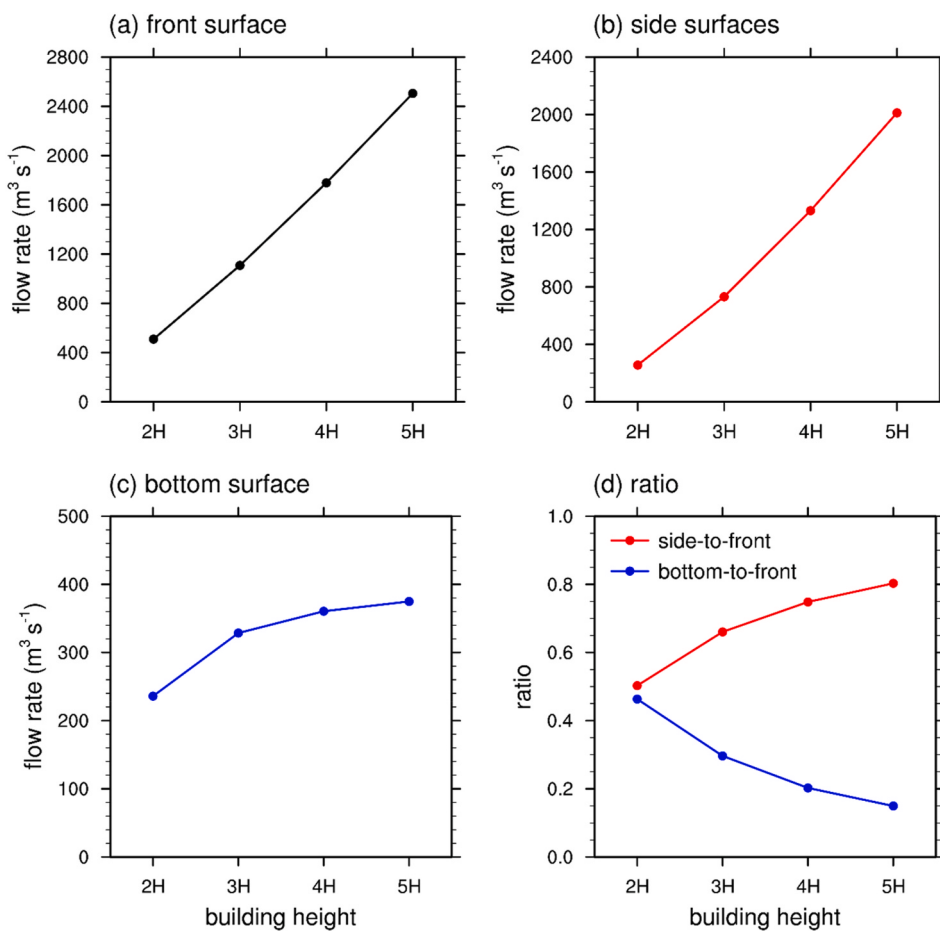


Fig. 4. Flow rates at the (a) front surface, (b) two side surfaces, and (c) bottom surface of a column as a function of tall-building height, and (d) the ratios of flow rate at the side surfaces to the flow rate at the front surface and flow rate at the bottom surface to the flow rate at the front surface as a function of tall-building height.

The increase of upper-level pollutant concentration behind a tall building has also been reported in previous studies (Han et al., 2017). At the pedestrian level (Fig. 5d, f, h, and j), the lowest pollutant concentration among W, L, S1, and S2 is seen in W, which is attributable to the intrusion of relatively clean air from the above. Flows passing through S1 and S2 carry less polluted air in W to L. In L, a relatively high pollutant concentration is seen near the leeward wall of the tall building. The pedestrian-level pollutant concentration in further downstream regions decreases compared with the 1H case.

Strong winds enhance ventilation. Thus, as the tall-building height increases, the pedestrian-level air quality near the tall building would be improved due to strengthened pedestrian-level winds. To examine tall-building effects on air quality, time- and area-averaged pollutant concentration at the pedestrian level is calculated for the five cases (Fig. 3b). Note that the region where pollutant concentration is averaged is identical to the region where wind speed is averaged (the blue square in Fig. 1b).

The tall-building height is normalized by H , and the pollutant concentration is normalized by q/U_H . As expected, as the tall-building height increases, the average pedestrian-level pollutant concentration decreases. The decreasing trend of the average pollutant concentration is almost perfectly fitted to a curve $y = 20.784 + 277.392 \exp(-1.476x)$, with the coefficient of determination higher than 0.999. We found that the data points of the two simulations with tall-building heights of 6H and 7H well lie on the fitting curve. As in the average pedestrian-level wind speed (Fig. 3a), the rate of change in the average pollutant concentration decreases with increasing tall-building height. Compared to the 1H case, the average pedestrian-level pollutant concentration is reduced by 58, 71, 74, and 76% in the 2H, 3H, 4H, and 5H cases,

respectively. That both the average wind speed and the average pollutant concentration show the decreasing tendencies of their rates of change suggests that the pedestrian-level pollutant dispersion is closely associated with the pedestrian-level flows.

The vertical profiles of time- and area-averaged pollutant concentrations in W, L, S1, and S2 are shown in Fig. 6. In all of W, L, S1, and S2, the average pollutant concentration at the pedestrian level decreases as the tall-building height increases. Among W, L, S1, and S2, W exhibits the largest difference in the average pollutant concentration at the pedestrian level between the 1H and 2H cases. In W, the average pollutant concentration decreases as the tall-building height increases below $z \sim 40$ m. In W, the vertical profiles of the average pollutant concentration in the 2H, 3H, 4H, and 5H cases exhibit a non-monotonic trend with height below $z = H$, which differs from the monotonic trends in L, S1, and S2. Between $z = 1.5$ m and the closest level to the ground surface ($z = 0.5$ m), the average pollutant concentration decreases with height, which seems to be associated with the transport of relatively clean air by downdrafts near the windward wall of the tall building. Above $z = 1.5$ m, the average pollutant concentration increases with height, reaches a local maximum (in the 2H, 3H, 4H, and 5H cases), and then decreases. In L, the decreasing trend of the average pollutant concentration at the pedestrian level with increasing tall-building height does not hold for upper levels (Fig. 6b). This is because pollutants are transported up to the levels just above the tall-building height for each case, which is suggested from the sharp decrease of pollutant concentration near the tall-building height. In S1, the vertical profiles of the average pollutant concentration between $z = 20$ m and 40 m resemble those in W, and above $z \sim 40$ m, the pollutant concentration is very low. The vertical profiles of the average pollutant concentration in S2 are

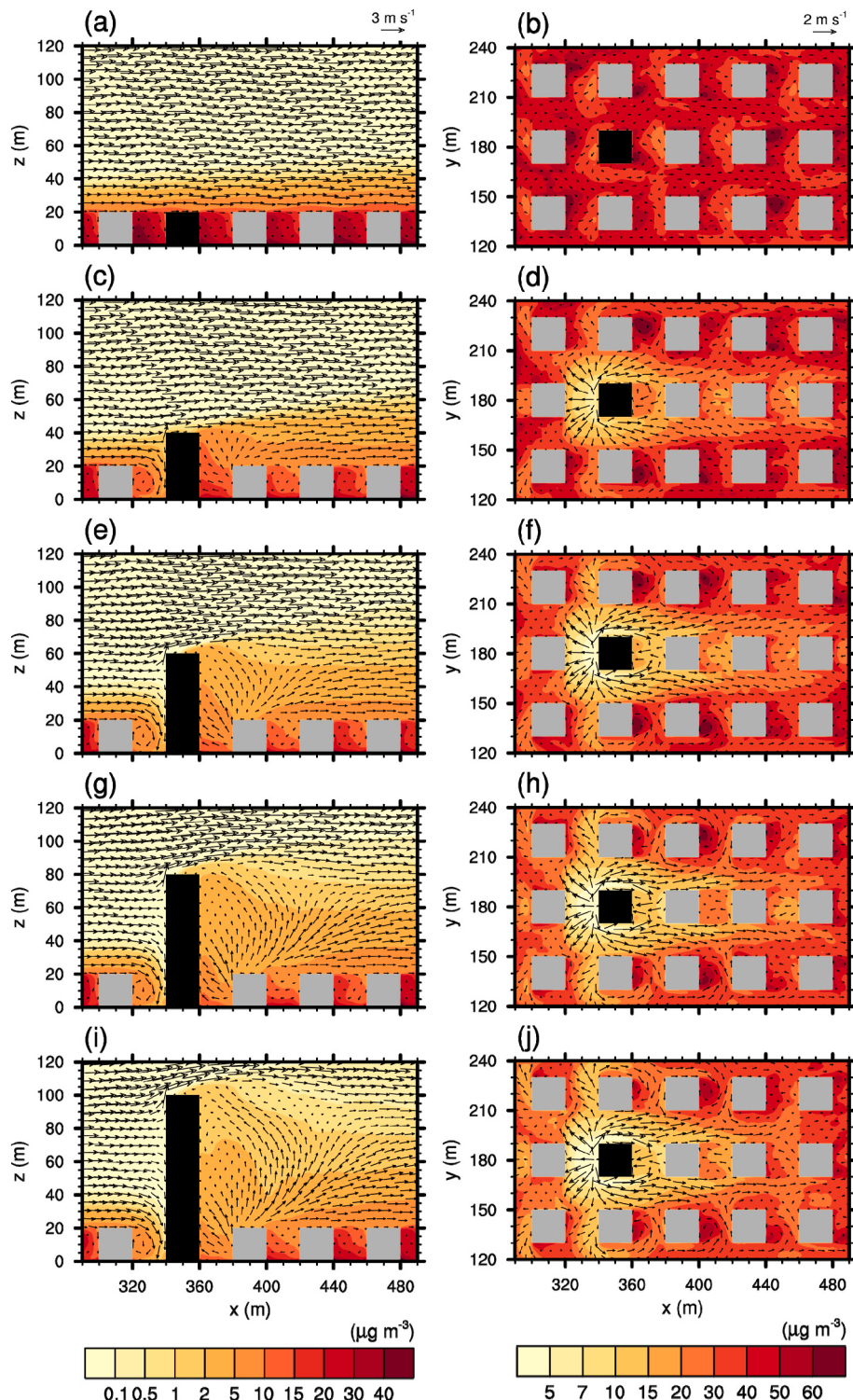


Fig. 5. Fields of time-averaged pollutant concentration and wind vector on the x - z plane at $y = 180$ m (left column) and on the x - y plane at $z = 1.5$ m (right column) in the (a, b) 1H, (c, d) 2H, (e, f) 3H, (g, h) 4H, and (i, j) 5H cases. The blocks in black indicate the tall buildings.

nearly the same as those in S1 (Fig. 6d). In addition to the four regions between the tall building and neighboring low-rise buildings that we focus on, there are another four $20\text{ m} \times 20\text{ m}$ regions excluding W, L, S1, and S2 in the blue square in Fig. 1b. Each of the vertical profiles of time- and area-averaged pollutant concentration in those four regions exhibits somewhat intermediate characteristics of the vertical profiles in the adjacent two regions (not shown).

The tall-building effects on pollutant dispersion discussed so far may

differ to some extent according to different settings such as the building configuration and inflow wind profile. Especially, if a change in building configuration changes the depth of the pollutant plume, the reduction of clean air supply may have some effects on the pollutant concentration near the tall building. To examine how the tall-building effects change under a different building configuration that changes the depth of the pollutant plume, five additional simulations where the number of building rows upstream of the tall building is increased from 6 to 12

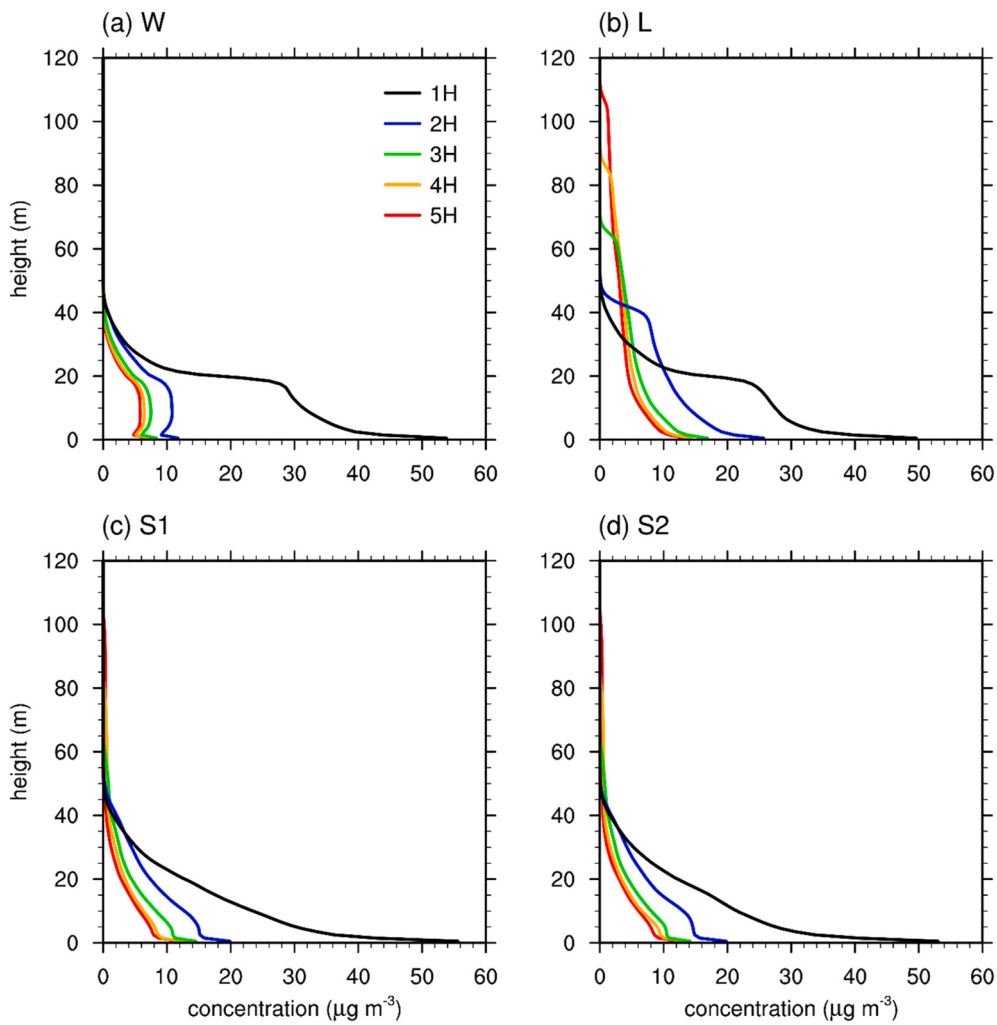


Fig. 6. Vertical profiles of time- and area-averaged pollutant concentrations in (a) W, (b) L, (c) S1, and (d) S2.

(hereafter, 12-row simulations) are performed and compared to the original simulations (hereafter, 6-row simulations). Fig. S2 shows fields of time-averaged pollutant concentration on the x - z plane at $y = 180$ m in the 6- and 12-row simulations when the tall-building height is $2H$. Compared to the 6-row simulation, it is clearly seen that the pollutant plume is deeper in the 12-row simulation. Near $x = 580$ m, the depth of the pollutant plume exceeds $2H$ (40 m) but is shallower than $3H$ (60 m) (Fig. S2b). Thus, the clean air supply downward into the street canyon in front of the tall building is reduced, which would lead to the weakening of the tall-building effect on pedestrian-level pollutant concentration. Fig. S3 shows the time- and area-averaged pollutant concentration near the tall building at $z = 1.5$ m as a function of tall-building height as in Fig. 3b but for the 12-row simulations. Although the average pollutant concentration is higher than that in the 6-row simulations for all cases, it has a decreasing trend with a decreasing rate of change according to the increase in tall-building height, which is similar to that for the 6-row simulations shown in Fig. 3b. The trend is fitted to a curve $y = 31.840 + 241.805 \exp(-1.460x)$ with the coefficient of determination being 0.996. The results indicate that the tall-building effects on pedestrian-level pollutant concentration are weakened but their dependence on the tall-building height holds for the cases with deeper pollutant plumes. The similarity between the trends is expectable because the upper air is still relatively clean than the lower air regardless of the depth of the pollutant plume. Further investigation is needed on whether the results would be similar in the simulations with different building configurations.

To examine the dependence of flow and pollutant concentration on the grid resolution, an additional simulation in which the grid size is doubled is performed. Fig. S4 shows fields of time-averaged pollutant concentration and wind vector on the x - y plane at $z = 1.5$ m in the 5H case. Because $z = 1.5$ m is not the prediction level in the simulation, the pollutant concentration and wind vector at $z = 1.5$ m are obtained by the linear interpolation between those at $z = 1$ m and $z = 3$ m. The patterns of time-averaged flow and pollutant concentration at the pedestrian level are similar to those shown in Fig. 5j, indicating that those time-averaged patterns are not largely affected by the doubling of grid size. The ratio of time- and area-averaged resolved TKE to time- and area-averaged resolved TKE is calculated for both simulations. The ratio vertically averaged between the surface and $z = 5H$ is 0.032 in the original simulation and 0.048 in the simulation with the doubled grid size, indicating that most of energy-containing eddies are resolved in both simulations. These show that the grid size of the original simulation is adequate to simulate the flow and pollutant dispersion around the tall building.

3.3. Instantaneous flow and pollutant dispersion

Next, we examine instantaneous flow and associated pollutant dispersion, focusing on coherent flow structure and its role in pollutant dispersion. Fig. 7 shows instantaneous pollutant concentration and wind vector fields on the x - z plane at $y = 180$ m in an upstream region of the tall building in the 5H case. The fields are plotted in 6-s intervals from t

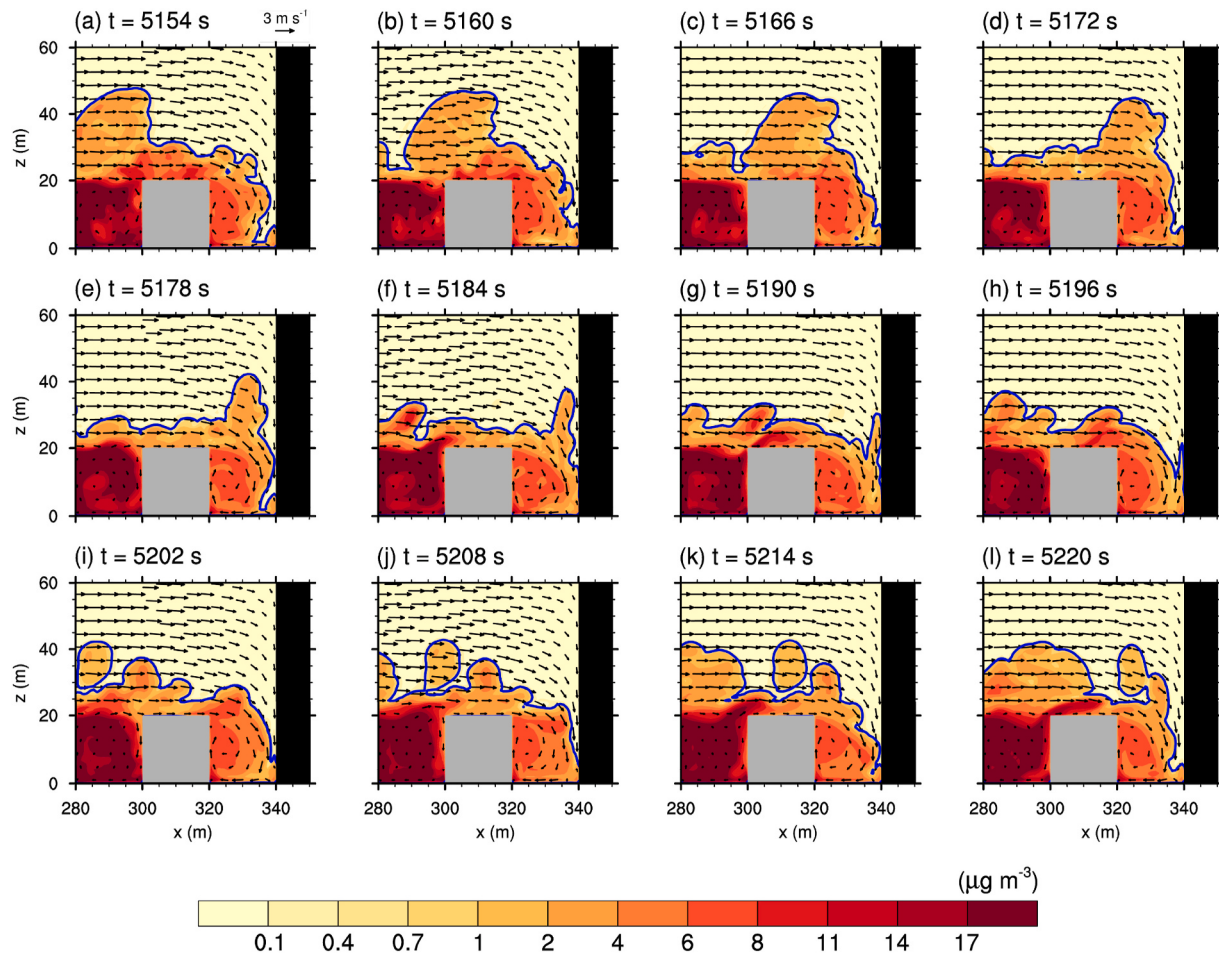


Fig. 7. Fields of pollutant concentration and wind vector on the x - z plane at $y = 180$ m and $t =$ (a) 5154, (b) 5160, (c) 5166, (d) 5172, (e) 5178, (f) 5184, (g) 5190, (h) 5196, (i) 5202, (j) 5208, (k) 5214, and (l) 5220 s in the upstream region of the tall building in the 5H case. The blue contour lines indicate the pollutant concentration of $0.5 \mu\text{g m}^{-3}$.

= 5154 s to 5220 s. Below $z = 20$ m, pollutants are more trapped in $280 \text{ m} < x < 300 \text{ m}$ than in $320 \text{ m} < x < 340 \text{ m}$. In $320 \text{ m} < x < 340 \text{ m}$, relatively clean air intrudes downward near the windward wall of the tall building and large amounts of pollutants are laterally dispersed. These cause the in-canyon pollutant concentration below $z = 20$ m to be lower in $320 \text{ m} < x < 340 \text{ m}$ than in $280 \text{ m} < x < 300 \text{ m}$. At $t = 5154$ s (Fig. 7a), a bulk of polluted air vertically extended over $z \sim 40$ m appears above $z = 20$ m in $280 \text{ m} < x < 300 \text{ m}$. The relatively clean air intruding downward near the windward wall of the tall building almost reaches the canyon bottom (see the $0.5 \mu\text{g m}^{-3}$ isoline in Fig. 7a). The bulk of polluted air moves downstream and passes over the top of the low-rise building located upstream of the tall building (Fig. 7b-d). Then, the bulk of polluted air is blocked by the tall building and then enters the canyon between the tall building and the low-rise building (Fig. 7e-g). Notably, there is a region of relatively polluted in-canyon air near the windward wall of the tall building at $t = 5184$ s and 5190 s compared with, for example, $t = 5154$ s. Afterward, the region near the windward wall of the tall building is newly filled with relatively clean air (Fig. 7h-l). From further upstream regions ($x < 280$ m), bulks of polluted air with various sizes and shapes appear. For example, a small bulk of polluted air which has moved from a further upstream region ($x < 280$ m) appears over the canyon in $280 \text{ m} < x < 300 \text{ m}$ at $t = 5202$ s, moves downstream, and is blocked by the tall building. At the same time, from a further upstream region ($x < 280$ m), a bulk of relatively polluted air moves downstream. The appearance, downstream movement, and intrusion of bulks of polluted air of various sizes and shapes are repeated. It is noteworthy that the pedestrian-level air quality near the

windward wall of the tall building temporarily deteriorates when the downward supply of relatively clean air that goes deep into the canyon is hindered. For example, at $x = 335.5$ m, the pedestrian-level pollutant concentration at $t = 5190$ s is $3.98 \mu\text{g m}^{-3}$ which is much larger than that at $t = 5154$ s ($0.18 \mu\text{g m}^{-3}$).

Fig. 8 is the same as Fig. 7 except for a downstream region of the tall building. The flow field in the downstream region of the tall building is more transient and complex than that in its upstream region (Figs. 7 and 8). A bulk of highly polluted air in the canyon between the tall building and the low-rise building located downstream of the tall building (see the $9 \mu\text{g m}^{-3}$ isoline in Fig. 8) changes its location, shape, and size with time. For example, a bulk of highly polluted air is mainly located in the downstream half of the canyon and extended upward at $t = 5166$ s, while it is mainly located in the upstream half of the canyon and rather extended horizontally at $t = 5196$ s. This feature seems to be associated with the evolutions of two vortices in the canyon which will be described later in this subsection. In $400 \text{ m} < x < 420 \text{ m}$, upward flow tends to prevail above the canyon and its intensity and direction change with time. The pollutant concentration there also changes with time, but its association with the upward flow seems to be complicated, needing further investigation.

Fig. 9 shows instantaneous pedestrian-level pollutant concentration and wind vector fields on the x - y plane at $z = 1.5$ m. In W, diverging flows near the windward wall of the tall building are persistently dominant and the pollutant concentration is low. The pollutant concentration near the windward wall of the tall building seems to be associated with the downward intrusion of clean air and its cut-off. For

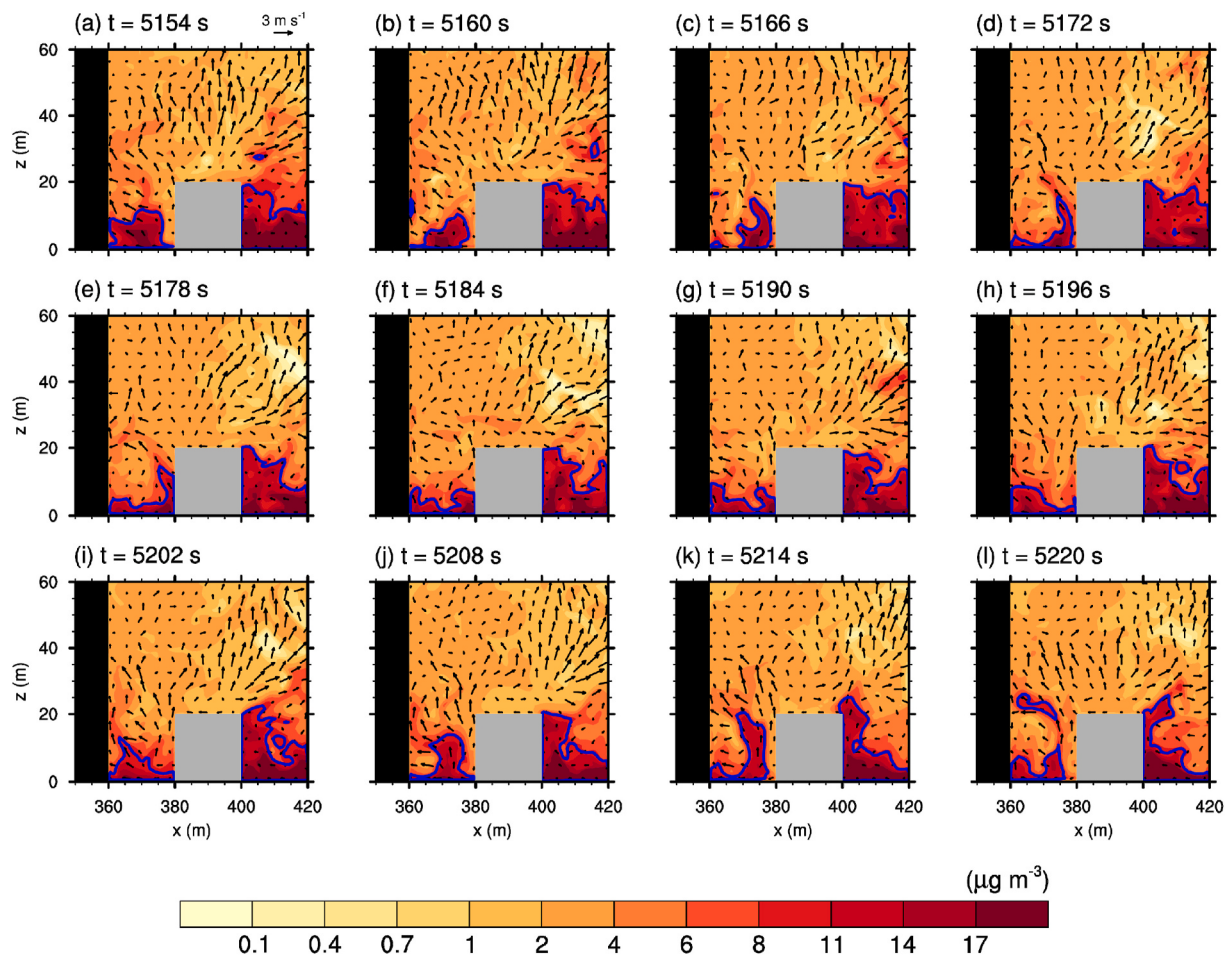


Fig. 8. Fields of pollutant concentration and wind vector on the x - z plane at $y = 180$ m and $t =$ (a) 5154, (b) 5160, (c) 5166, (d) 5172, (e) 5178, (f) 5184, (g) 5190, (h) 5196, (i) 5202, (j) 5208, (k) 5214, and (l) 5220 s in the downstream region of the tall building in the 5H case. The blue contour lines indicate the pollutant concentration of $9 \mu\text{g m}^{-3}$.

example, the pollutant concentration there is low at $t = 5154$ s when the clean air intrudes deep into the canyon (Fig. 7a), while it is relatively high at $t = 5190$ s when the clean air intrusion is hindered (Fig. 7g). In S1 and S2, the pollutant concentration is low near the side walls of the tall building while it is high in the rest of the regions. In L, at $t = 5154$ s, there are a large counter-clockwise vortex dominating the canyon and a small clockwise vortex near one of the leeward corners of the tall building ($(x, y) = (360 \text{ m}, 190 \text{ m})$) (Fig. 9a). Pollutants are trapped by the vortices, resulting in high pollutant concentrations in the vortices. The large counter-clockwise vortex moves downstream while decreasing its size, and the small clockwise vortex expands along the leeward wall (Fig. 9b-d). The large counter-clockwise vortex disappears after reaching the windward wall of the low-rise building behind the tall building, and the small clockwise vortex further expands (Fig. 9e-h). At $t = 5202$ s, the expanded clockwise vortex dominates the canyon and a small counter-clockwise vortex is newly formed at the corner at $(x, y) = (360 \text{ m}, 170 \text{ m})$ (Fig. 9i). The pollutant concentrations in the two vortices are high. The small counter-clockwise vortex expands along the leeward wall of the tall building, and the large clockwise vortex moves downstream while decreasing its size (Fig. 9j-l). The newly formed vortices go through the processes of expansion, movement, and disappearance, exhibiting time-varying flow features in L. Fig. 9 indicates that in L, the temporal variation of the two counter-rotating vortices greatly affects the pedestrian-level pollutant concentration.

To examine the temporal variations of the pedestrian-level pollutant concentration distribution near the tall building, the Hovmöller diagrams of normalized pollutant concentration deviation at $y = 180$ m and

$z = 1.5$ m in W and L are plotted (Fig. 10). The Hovmöller diagram represents the change in the spatial distribution of a certain variable over time. The deviation from time- and line-averaged ($320 \text{ m} \leq x \leq 340 \text{ m}$ in Fig. 10a and $360 \text{ m} \leq x \leq 380 \text{ m}$ in Fig. 10b) pollutant concentration is normalized by its standard deviation. In W, the large negative pollutant concentration deviation is seen in the region slightly away from $x = 340$ m, which is caused by the downward intrusion of relatively clean air near the windward wall of the tall building. Near $x = 320$ m, a large positive pollutant concentration deviation is seen, which is a result of the transport of pollutants toward the low-rise building in front of the tall building due to the diverging flow. Band-like patterns of negative and positive deviations of pollutant concentration that are slightly slanted from the streamwise direction are distinct. The band-like patterns are repeated although their appearances do not seem to be periodic. The band-like patterns of negative deviations are associated with the transport of relatively less polluted air from the region near the windward wall of the tall building heading upstream when a deep intrusion of clean air into the canyon occurs. On the other hand, the band-like patterns of positive deviations are associated with the transport of relatively more polluted air that has intruded downward into the canyon toward the low-rise building in front of the tall building. The spots of positive deviation of pollutant concentration adjacent to the windward wall of the tall building indicate pollutant trapping in a small counter-clockwise vortex. The pollutant trapping in a bottom corner vortex was also reported in an LES study (Park et al., 2022). In L, the patterns of deviations of pollutant concentration are more complicated than those in W. These patterns are closely related to the temporal

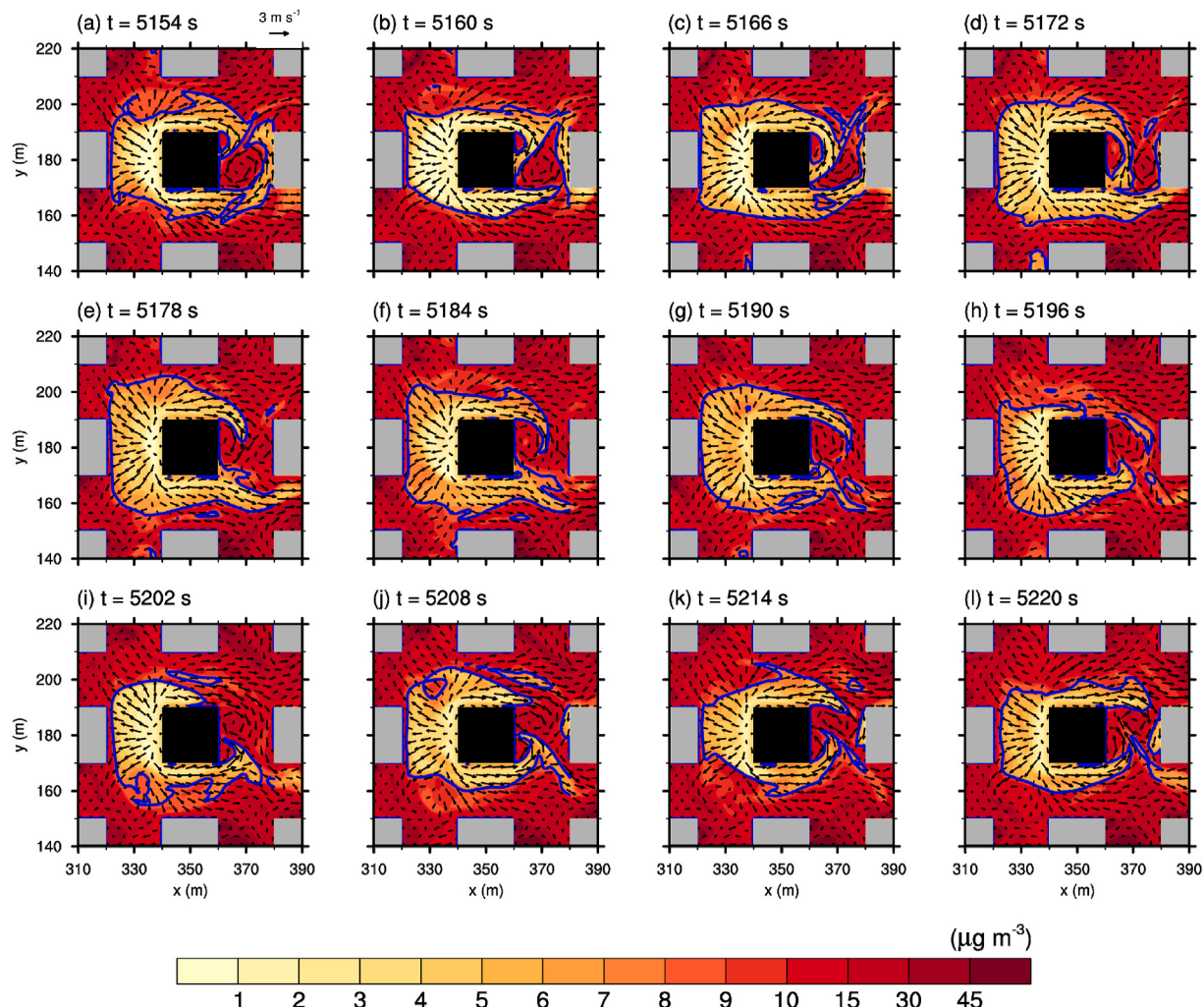


Fig. 9. Fields of pollutant concentration and wind vector on the x - y plane at $z = 1.5$ m and $t =$ (a) 5154, (b) 5160, (c) 5166, (d) 5172, (e) 5178, (f) 5184, (g) 5190, (h) 5196, (i) 5202, (j) 5208, (k) 5214, and (l) 5220 s in the 5H case. The blue contour lines indicate the pollutant concentration of $8 \mu\text{g m}^{-3}$.

evolution of the two counter-rotating vortices in this region (Fig. 9). For example, from $t \sim 5100$ s to 5220 s, two band-like patterns of positive deviation toward the upper-right direction appear and negative deviations are seen between them. Each of the band-like patterns of positive deviation is associated with the development of a vortex near the leeward wall of the tall building and its downstream movement. The first of the two band-like patterns of positive deviation indicates the large counter-clockwise vortex moving downstream and decreasing its size from $t = 5154$ s to 5172 s shown in Fig. 9a–d.

To examine whether periodicity exists in the temporal variations of pollutant concentration, the power spectral density of pollutant concentration is calculated at one point in W and another point in L at $y = 180$ m and $z = 1.5$ m (Fig. S5). At the point in W, the power spectrum of pollutant concentration shows a big contrast between the cases with and without a tall building. Compared to the 1H case, the power spectral densities at relatively large (small) periods are smaller (larger) in the 2H, 3H, 4H, and 5H cases, indicating that the presence of a tall building suppresses pollutant concentration variations of long time scales and enhances those of short time scales. Under the presence of a tall building, a change in the height of the tall building does not seem to significantly affect the time scale of pollutant concentration variation. The absence of pronounced peak in the power spectrums indicates that there is no obvious periodicity in pollutant concentration variations in W. At the point in L, the changes in the power spectrum according to the tall-building height are relatively gradual compared to the dramatic change

from the 1H to 2H case at the point in W. As the tall-building height increases, pollutant concentration variations of long time scales are overall suppressed and those of short time scales are overall enhanced. No pronounced peak is found in the power spectrums in the 2H, 3H, 4H, and 5H cases, indicating that as in W, there is no obvious periodicity in pollutant concentration variations in L. Fig. S5 indicates that the processes associated with the variations of pollutant concentration addressed in Figs. 7–9 are repeated but do not have an obvious periodicity.

4. Summary and conclusions

In this study, we examined the effects of a tall building on pedestrian-level flow and pollutant dispersion using an LES model. As the tall-building height increases, the time- and area-averaged wind speed at the pedestrian level increases and the rate of change in the average wind speed decreases. The decreasing trend of the rate of change in the average pedestrian-level wind speed with increasing tall-building height is attributable to an increasing tendency of the oncoming flow to pass by the sides of the tall building rather than going down. The time- and area-averaged pollutant concentration at the pedestrian level and the rate of change in the average pollutant concentration decrease with increasing tall-building height. Instantaneous flow and pollutant dispersion were also analyzed. In the upstream region of the tall building, bulks of polluted air repeatedly appearing from the upstream region move

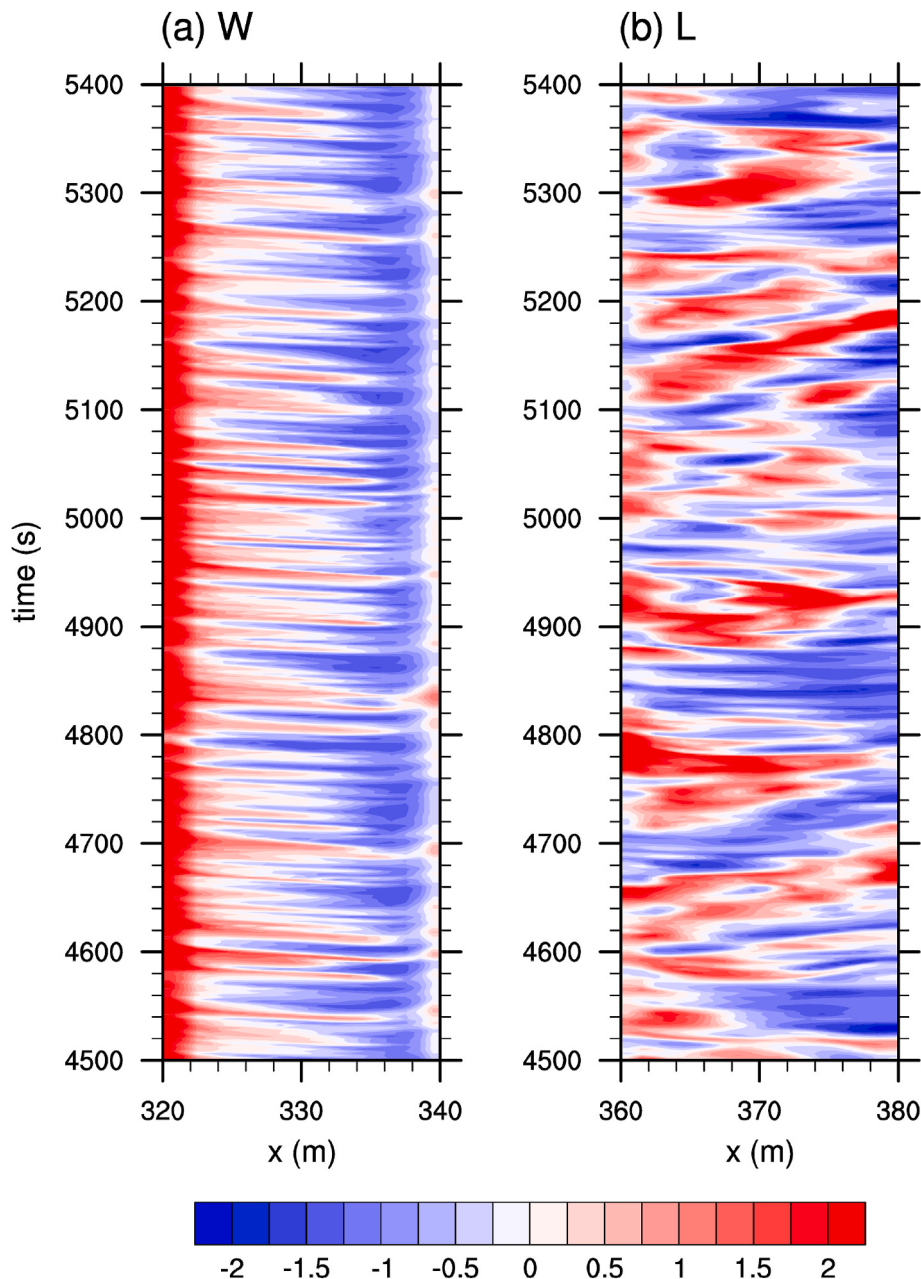


Fig. 10. Hovmöller diagrams of normalized pollutant concentration deviation at $y = 180$ m and $z = 1.5$ m in (a) W and (b) L in the 5H case. The pollutant concentration deviation from time- and line-averaged pollutant concentration is normalized by its standard deviation.

downstream and enter the canyon between the tall building and the low-rise building located upstream of the tall building, temporarily degrading the pedestrian-level air quality. In the downstream region of the tall building, at the pedestrian level, two counter-rotating vortices exist in the canyon just behind the tall building. Each of the vortices repeatedly develops at one of the leeward corners of the tall building, moves downstream, and finally disappears. The repeated processes of two vortices from formation to disappearance largely affect the pedestrian-level flow and pollutant concentration in the leeward side of the tall building.

This study considered an idealized building configuration of a tall building and surrounding low-rise buildings. Tall-building effects on flow and pollutant dispersion can differ depending on building configurations. Further studies with various idealized and real urban configurations are needed. This study neglected thermal effects on flow and pollutant dispersion. If the solar radiation directs to the windward

(leeward) wall of a tall building, the downdrafts (updrafts) near its windward (leeward) wall can be suppressed (enhanced) due to surface heating. The thermal effects deserve investigation.

Credit author statement

Jong-Won Kim: Validation, Formal analysis, Investigation, Data curation, Writing – original draft, Visualization. **Jong-Jin Baik:** Conceptualization, Formal analysis, Writing – original draft, Writing – review & editing, Supervision. **Beom-Soon Han:** Conceptualization, Formal analysis, Investigation, Writing – review & editing. **Joohyun Lee:** Formal analysis, Investigation, Writing – review & editing. **Han-Gyul Jin:** Formal analysis, Writing – original draft, Writing – review & editing. **Kyeongjoo Park:** Validation, Formal analysis, Writing – review & editing. **Hyeji Yang:** Formal analysis, Investigation. **Seung-Bu Park:** Formal analysis, Writing – review & editing.

Declaration of competing interest

The authors declare that they have no known competing financial interests or personal relationships that could have appeared to influence the work reported in this paper.

Acknowledgements

The authors are grateful to three anonymous reviewers for providing valuable comments on this work. This research did not receive any specific grant from funding agencies in the public, commercial, or not-for-profit sectors.

Appendix A. Supplementary data

Supplementary data to this article can be found online at <https://doi.org/10.1016/j.apr.2022.101500>.

References

- Architectural Institute of Japan (AIJ), 2016. AIJ Benchmarks for Validation of CFD Simulations Applied to Pedestrian Wind Environment Around Buildings. Architectural Institute of Japan, Tokyo.
- Brixey, L.A., Heist, D.K., Richmond-Bryant, J., Bowker, G.E., Perry, S.G., Wiener, R.W., 2009. The effect of a tall tower on flow and dispersion through a model urban neighborhood Part 2. Pollutant dispersion. *J. Environ. Monit.* 11, 2171–2179.
- Buccolieri, R., Sandberg, M., Di Sabatino, S., 2010. City breathability and its link to pollutant concentration distribution within urban-like geometries. *Atmos. Environ.* 44, 1894–1903.
- CTBUH. <https://ctbuh.org>. (Accessed 2 January 2022).
- Deardorff, J.W., 1980. Stratocumulus-capped mixed layers derived from a three-dimensional model. *Boundary-Layer Meteorol.* 18, 495–527.
- Fuka, V., Xie, Z.-T., Castro, I.P., Hayden, P., Carpentieri, M., Robins, A.G., 2018. Scalar fluxes near a tall building in an aligned array of rectangular buildings. *Boundary-Layer Meteorol.* 167, 53–76.
- Grantz, D.A., Garner, J.H.B., Johnson, D.W., 2003. Ecological effects of particulate matter. *Environ. Int.* 29, 213–239.
- Han, B.-S., Baik, J.-J., Kwak, K.-H., Park, S.-B., 2018. Large-eddy simulation of reactive pollutant exchange at the top of a street canyon. *Atmos. Environ.* 187, 381–389.
- Han, B.-S., Park, S.-B., Baik, J.-J., Park, J., Kwak, K.-H., 2017. Large-eddy simulation of vortex streets and pollutant dispersion behind high-rise buildings. *Q. J. R. Meteorol. Soc.* 143, 2714–2726.
- Hang, J., Li, Y., Sandberg, M., Buccolieri, R., Di Sabatino, S., 2012. The influence of building height variability on pollutant dispersion and pedestrian ventilation in idealized high-rise urban areas. *Build. Environ.* 56, 346–360.
- Heist, D.K., Brixey, L.A., Richmond-Bryant, J., Bowker, G.E., Perry, S.G., Wiener, R.W., 2009. The effect of a tall tower on flow and dispersion through a model urban neighborhood Part 1. Flow characteristics. *J. Environ. Monit.* 11, 2163–2170.
- Huang, X., Gao, L., Guo, D., Yao, R., 2021. Impacts of high-rise building on urban airflows and pollutant dispersion under different temperature stratifications: numerical investigations. *Atmos. Pollut. Res.* 12, 100–112.
- Kampa, M., Castanas, E., 2008. Human health effects of air pollution. *Environ. Pollut.* 151, 362–367.
- Kikumoto, H., Ooka, R., Han, M., Nakajima, K., 2018. Consistency of mean wind speed in pedestrian wind environment analyses: mathematical consideration and a case study using large-eddy simulation. *J. Wind Eng. Ind. Aerod.* 173, 91–99.
- Kim, K.-H., Kabir, E., Kabir, S., 2015. A review on the human health impact of airborne particulate matter. *Environ. Int.* 74, 136–143.
- Maronga, B., Banzhaf, S., Burmeister, C., Esch, T., Forkel, R., Fröhlich, D., Fuka, V., Gehrke, K.F., Geletić, J., Giersch, S., Gronemeier, T., Grob, G., Heldens, W., Hellsten, A., Hoffmann, F., Inagaki, A., Kadash, E., Kanani-Sühring, F., Ketelsen, K., Khan, B.A., Knigge, C., Knoop, H., Krč, P., Kurppa, M., Maamari, H., Matzarakis, A., Mauder, M., Pallasch, M., Pavlik, D., Pfafferott, J., Resler, J., Rissmann, S., Russo, E., Salim, M., Schrempf, M., Schwenkel, J., Seckmeyer, G., Schubert, S., Sühring, M., von Tils, R., Vollmer, L., Ward, S., Witha, B., Wurps, H., Zeidler, J., Raasch, S., 2020. Overview of the PALM model system 6.0. *Geosci. Model Dev.* 13, 1335–1372.
- Mei, S.-J., Hu, J.-T., Liu, D., Zhao, F.-Y., Li, Y., Wang, Y., Wang, H.-Q., 2017. Wind driven natural ventilation in the idealized building block arrays with multiple urban morphologies and unique package building density. *Energy Build.* 155, 324–338.
- Moeng, C.-H., Wyngaard, J.C., 1988. Spectral analysis of large-eddy simulations of the convective boundary layer. *J. Atmos. Sci.* 45, 3573–3587.
- Park, S.-B., Baik, J.-J., Han, B.-S., 2015. Large-eddy simulation of turbulent flow in a densely built-up urban area. *Environ. Fluid Mech.* 15, 235–250.
- Park, S.-B., Baik, J.-J., Han, B.-S., 2022. Coherent flow structures and pollutant dispersion in a street canyon. *Boundary-Layer Meteorol.* 182, 363–378.
- Park, S.-B., Baik, J.-J., Ryu, Y.-H., 2013. A large-eddy simulation study of bottom-heating effects on scalar dispersion in and above a cubical building array. *J. Appl. Meteorol. Climatol.* 52, 1738–1752.
- Raasch, S., Schröter, M., 2001. PALM - a large-eddy simulation model performing on massively parallel computers. *Meteorol. Z.* 10, 363–372.
- Razak, A.A., Hagishima, A., Ikegaya, N., Tanimoto, J., 2013. Analysis of airflow over building arrays for assessment of urban wind environment. *Build. Environ.* 59, 56–65.
- Resler, J., Eben, K., Geletić, J., Krč, P., Rosecký, M., Sühring, M., Belda, M., Fuka, V., Halenka, T., Huszár, P., Karlický, J., Benesová, N., Doubalová, J., Honzáková, K., Keder, J., Nápravníková, Š., Vlček, O., 2021. Validation of the PALM model system 6.0 in a real urban environment: a case study in Dejvice, Prague, the Czech Republic. *Geosci. Model Dev.* 14, 4797–4842.
- Saiki, E.M., Moeng, C.-H., Sullivan, P.P., 2000. Large-eddy simulation of the stably stratified planetary boundary layer. *Boundary-Layer Meteorol.* 95, 1–30.
- Santiago, J.L., Martilli, A., Martín, F., 2007. CFD simulation of airflow over a regular array of cubes. Part 1: three-dimensional simulation of the flow and validation with wind-tunnel measurements. *Boundary-Layer Meteorol.* 122, 609–634.
- Squires, F.A., Nemitz, E., Langford, B., Wild, O., Drysdale, W.S., Acton, W.J.F., Fu, P., Grimson, C.S.B., Hamilton, J.F., Hewitt, C.N., Hollaway, M., Kotthaus, S., Lee, J., Metzger, S., Pingintha-Durden, N., Shaw, M., Vaughan, A.R., Wang, X., Wu, R., Zhang, Q., Zhang, Y., 2020. Measurements of traffic-dominated pollutant emissions in a Chinese megacity. *Atmos. Chem. Phys.* 20, 8737–8761.
- Stevens, C.J., Bell, J.N.B., Brimblecombe, P., Clark, C.M., Duse, N.B., Fowler, D., Lovett, G.M., Wolseley, P.A., 2020. The impact of air pollution on terrestrial managed and natural vegetation. *Philos. Trans. R. Soc. A.* 378, 20190317.
- Tamura, Y., Xu, X., Yang, Q., 2019. Characteristics of pedestrian-level mean wind speed around square buildings: effects of height, width, size and approaching flow profile. *J. Wind Eng. Ind. Aerod.* 192, 74–87.
- Tominaga, Y., Mochida, A., Shirasawa, T., Yoshie, R., Kataoka, H., Harimoto, K., Nozu, T., 2004. Cross comparisons of CFD results of wind environment at pedestrian level around a high-rise building and within a building complex. *J. Asian Architect. Build. Eng.* 3, 63–70.
- Wang, H., Ngan, K., 2021. Effects of inhomogeneous ground-level pollutant sources under different wind directions. *Environ. Pollut.* 289, 117903.
- Wicker, L.J., Skamarock, W.C., 2002. Time-splitting methods for elastic models using forward time schemes. *Mon. Weather Rev.* 130, 2088–2097.
- Williamson, J.H., 1980. Low-storage Runge-Kutta schemes. *J. Comput. Phys.* 35, 48–56.